BIOCHEMISTRY
including biophysical chemistry & molecular biology

Article

pubs.acs.org/biochemistry

How Does a Registry Change in Dynein's Coiled-Coil Stalk Drive Binding of Dynein to Microtubules?

Junghyun Choi, Hahnbeom Park, and Chaok Seok*

Department of Chemistry, Seoul National University, Seoul 151-747, Republic of Korea

Supporting Information

ABSTRACT: Dynein is a motor protein that transports cellular cargo along the microtubule (MT) by consuming ATP. Dynein's microtubule-binding domain (MTBD) is separated from the ATP-binding core by a ~15 nm stalk that consists of two α-helices forming an antiparallel coiled coil. It was previously suggested that the coiled-coil stalk creates a registry shift to modulate its binding affinity for MT. A crystal structure of the low-affinity form of MTBD was determined, but that of the high-affinity form with the registry shift is not yet available. In this study, we obtained an all-atom model structure for the high-affinity form of MTBD bound to MT by an anisotropic network model, protein−protein docking, and molecular dynamics simulations. We observe that the magnitude of the coiled-coil helix sliding is dramatically reduced near the two prolines that form the stalk−MTBD boundary and subsequently transformed to cyclic movements of MTBD helices, leading to formation of a new salt bridge with MT at the binding interface. The proposed mechanism explains the roles of highly conserved residues such as the two prolines at the stalk−MTBD boundary, the nonpolar tryptophan and proline residues near the binding interface, and the electropositive residues forming salt bridges with MT.

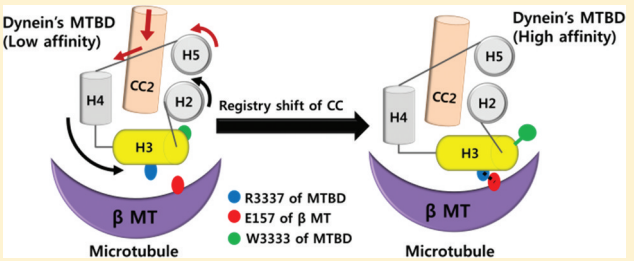

Dyneins are cytoskeletal motor proteins that power cellular motility through ATP hydrolysis.[1,2] Cytoskeletal motor proteins, including dynein, kinesin, and myosin, carry various types of cargo along the cytoskeleton and are involved in many cellular processes.[3−5] Unlike in kinesin or myosin, the microtubule-binding domain (MTBD) of dynein is separated by a long distance (~15 nm) from the ATP-binding core.[6,7] Several human diseases such as neural degeneration[8] and male infertility[9] are related to dynein dysfunction.

Recently, a crystal structure of MTBD of mouse cytoplasmic dynein was determined for a construct that does not show high affinity for microtubules.[7] The crystal structure of MTBD, as shown in Figure 1a, is composed of a globular bundle of six helices (H1−H6) and a long coiled-coil (CC) stalk that connects the helix bundle to the ATP-binding, AAA+ domain. The coiled-coil stalk consists of two antiparallel helices. One helix (CC1) extends from the AAA+ domain to H1 and the other helix (CC2) from H6 to AAA+. A low-resolution pose of MTBD on MTs was obtained by fitting the low-affinity MTBD structure to a cryo-electron microscopy (cryo-EM) density map[7,11] (Figure 1b). However, the atomic-level picture of MTBD−MT binding still remains to be elucidated.

Although the high-resolution structure of the MTBD−MT complex is unknown, some molecular-level information about MTBD−MT binding is available. First, it has been suggested by a disulfide cross-linking experiment[12] and a fusion experiment with seryl tRNA-synthetase[13] that the binding affinity of MTBD for MT is controlled by a registry change in the two helices of the coiled-coil stalk. In other words, sliding movement of a helix against the other by a single helix turn induces binding of MTBD to MT. Second, several MTBD residues were shown to be critical for binding by a mutagenesis experiment.[14] Because those key residues form an electropositive surface when mapped onto the crystal structure of MTBD, it is assumed that binding of MTBD to MT is stabilized by strong electrostatic interaction with the electronegative surface of MT.[14,15] This information is not enough to explain MTBD−MT binding in atomic detail, and the following questions are raised. Why is the crystal structure of MTBD (in the low-affinity state by construction) with the positively charged surface not enough for MT binding? What kind of changes in MTBD are necessary for MT binding? How does the sliding of the coiled-coil helices drive changes necessary for MT binding? Why does the mutation of the highly conserved, hydrophobic residue W3333 diminish the binding affinity for MT? In this work, we attempt to answer these questions through a computational approach.

Several computational modeling techniques were utilized in this study. First, the conformational changes of MTBD induced by stalk helix sliding were predicted by using the anisotropic network model (ANM) method.[16] Next, the resulting MTBD model structure that represents the high-affinity state was docked onto a tubulin protofilament structure, and the docked complex structure was refined to allow conformational changes at the binding interface. In the high-affinity model structure, the magnitude of the helix sliding of CC1 and CC2 due to the

Received: May 31, 2011
Revised: July 16, 2011
Published: August 2, 2011

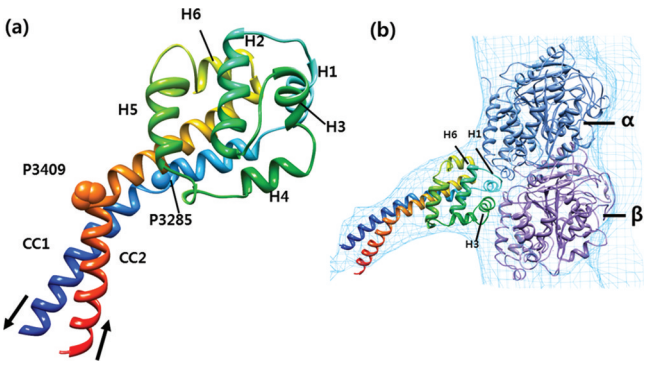

Figure 1. Structure of dynein's microtubule-binding domain (MTBD). (a) Low-affinity crystal structure of MTBD of the cytoplasmic mouse dynein (chain A of PDB entry 3ERR).[7] The globular helix bundle consists of six α-helices denoted by H1−H6, which is connected by the coiled-coil stalk helices (CC1 and CC2) to the ATP-binding AAA + domain (not shown here). Kinks on CC1 and CC2 appear at highly conserved prolines (P3285 and P3409). CC1 and CC2 have been suggested to undergo a registry shift (shown as black arrows at the bottom left) to induce microtubule (MT) binding.[10] (b) Low-resolution model for the MTBD−MT complex structure obtained by fitting the low-affinity crystal MTDB structure and a tubulin protofilament structure (α-tubulin, light blue; β-tubulin, light purple)[7] to the cryo-EM map.[7,11,21] α- and β-tubulin compose the basic unit of MTs, a repeat of which forms the long microtubule. Three MTBD helices (H1, H3, and H6) make contact with the groove formed at the interface of α- and β-tubulin.

registry shift drops suddenly from ~4.5 to ~2 Å near the highly conserved proline residues at the stalk−MTBD boundary, and this leads to a series of cyclic movements of H4, H3, and H2. The most significant change observed from modeling is the lateral movement of helix H3 at the MTBD−MT binding interface, which drives formation of a new salt bridge between R3337 of H3 and E157 of the MT β-unit. Further molecular dynamics (MD) simulations suggest that the highly conserved W3333 residue plays the important role of a linchpin, maintaining the position of H3 by hydrophobic interaction with another highly conserved residue, P3311.

METHODS

Modeling of the High-Affinity MTBD Structure Using ANM. A model structure for the high-affinity state of MTBD (termed $MTBD_{HA}$) was obtained by applying the anisotropic network model (ANM)[16,17] method to the crystal structure (chain A from PDB entry 3ERR) of the low-affinity state structure (termed $MTBD_{LA}$) of mouse cytoplasmic dynein. Normal modes were obtained by considering an elastic network of 168 C_α atoms (from E3260 to K3427) that are connected by harmonic springs with other C_α atoms within 7 Å.[18] A number of low-frequency modes correspond to swing motions of the coiled-coil stalk rather than sliding. To describe the coiled-coil sliding motion, we selected 20 normal modes showing the strongest correlation with the CC1−CC2 sliding motion and found the optimal linear combination of the selected modes by maximizing the correlation with CC1−CC2 sliding. The C_α coordinates of the initial MTBD structure were then perturbed slightly by adding the resulting normalized motion vector multiplied by 1 Å. This procedure was repeated by using the perturbed structure in the previous step as the initial structure in the next step until the C_α atoms in the coiled-coil (CC) helix pairs move as much as a single helix turn (~4.5 Å).[8] The idea of applying normal mode motions iteratively was also employed in other studies.[19] An all-atom model $MTBD_{HA}$ structure was finally constructed from the C_α model structure obtained from ANM and the all-atom $MTBD_{LA}$ structure using MODELLER.[20]

Computational Docking of MTBD to MT. The model $MTBD_{HA}$ structure was docked onto the crystal structure of a tubulin protofilament (PDB entry 1JFF) to obtain a model MTBD−MT complex structure. First, the MTBD and MT proteins were fit into a cryo-EM map (EMDB[21] entry 1581) using the EM fitting module of UCSF Chimera.[8] The resulting complex structure was used as the initial structure for refinement docking simulations using an in-house docking program and RosettaDock.[22] The refinement docking simulations allow conformational changes induced by binding. First, 100 independent Monte Carlo minimization simulations[23] with simulated annealing[24] were performed starting from the initial structure using an in-house program. During the simulations, trial moves of the MTBD helices at the putative binding interface (H1, H3, and H6 in Figure 1) were generated in the direction of ANM normal modes. The docking energy function consists of Lennard-Jones potential, Coulomb potential, hydrogen bonding energy,[25] and a potential for solvent accessible surface area.[26] From the 100 refined complex structures, 10 structures that have the largest number of interprotein contacts were selected. The number of interprotein contacts rather than total energy was used as a rough criterion for selecting candidates for further refinement because side chain conformation is not intensively optimized at this stage. Finally, these complexes were further refined using RosettaDock with default parameters except for reducing the rigid-body perturbation sizes from (3, 8, 8) to (0.1, 0.1, 1) to maintain the overall poses obtained in the previous stage. For each of the 10 starting complex models, 100 refined models were generated, giving 1000 models for the $MTBD_{HA}$−MT complex. For a comparative study, 100 RosettaDock-refined complex models starting from the EM map-fitted $MTBD_{LA}$−MT complex structure were also generated.

From each set of generated structures for the $MTBD_{HA}$−MT and $MTBD_{LA}$−MT complexes, the best complex structure was selected using the RosettaDock refinement score after filtering out the structures with fewer than eight intermolecular, charged hydrogen bonds and those for which the fitness score[27] of the final docked pose was <0.054 when fitted to the cryo-EM map. Charged hydrogen bonds are defined as those involving a hydrogen donor of a positively charged residue at neutral pH (Arg and Lys) and a hydrogen acceptor of a negatively charged residue at neutral pH (Glu and Asp) in which the distance between the H atom and hydrogen acceptor is <3.5 Å and the angle formed by the hydrogen donor, hydrogen, and hydrogen acceptor is >120°. This criterion for the number of charged hydrogen bonds was introduced to focus on model structures with a sufficient number of intermolecular salt bridges that are supposed to play key roles in formation of the complex.

Molecular Dynamics Simulations of the MTBD−MT Complex. To investigate the atomic interactions and dynamics at the complex interface in more detail, 6 ns MD simulations were performed starting from the model structures for both $MTBD_{HA}$−MT and $MTBD_{LA}$−MT complexes. Additional MD simulation for the W3333A mutant starting from the $MTBD_{HA}$−MT complex structure was also performed to understand the role of the highly conserved tryptophan

dx.doi.org/10.1021/bi200834k | Biochemistry 2011, 50, 7629−7636

residue. All simulations were conducted using AMBER10.[28] The temperature was set to 300 K using Langevin dynamics, while the pressure was set to 1 bar using a Berendsen barostat.[29] AMBER99SB parameters and SHAKE[30] were applied to the protein, while water molecules were considered explicitly with the TIP3P model.[31] For efficient simulations, those regions away from the binding interface were removed from the system (coiled-coil residues beyond P3285 and P3409 for MTBD and residues that do not belong to any secondary structure segments or connecting loops at the binding interface for MT), and restraints were applied to all pairs of backbone N atoms within 15 Å for both the MT and MTBD coiled coil using the NMR restraint tool in the AMBER package to maintain the overall intramolecular structure during simulations. We analyzed the full 6 ns MD trajectories except for that of the W3333A mutant, for which the final 3.7 ns trajectory was analyzed because a conformational change in R3337 occurs at 2.3 ns.

RESULTS AND DISCUSSION

Overall Structure and Binding Affinity of the MTBD−MT Complex. As described above, the model structure for MTBD in the high-affinity state ($MTBD_{HA}$) was generated by imposing the registry shift of the coiled-coil helices on the MTBD crystal structure in the low-affinity state ($MTBD_{LA}$). It was therefore first confirmed that the $MTBD_{HA}$ structure indeed has a registry shift in the final model, as shown in Figure 2.

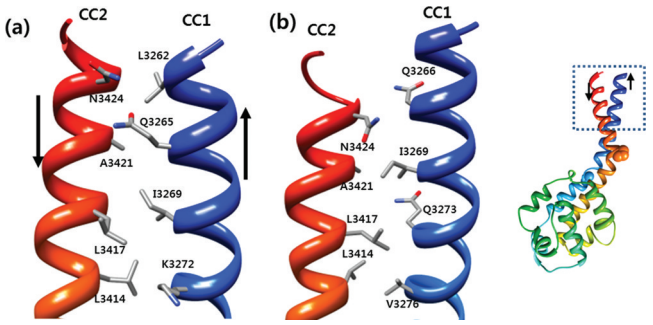

Figure 2. Shift of the coiled-coil registry from (a) that of the crystal $MTBD_{LA}$ structure to (b) that of the model $MTBD_{HA}$ structure at the region indicated with the dashed box on the right. The directions of helix movements are indicated with arrows.

This registry change induces conformational changes in the helix bundle (from H1 to H6), and the changes will be discussed in more detail in the next subsection.

Both complex model structures, $MTBD_{HA}$−MT and $MTBD_{LA}$−MT, generated by EM map fitting and subsequent refinement docking fit well to the cryo-EM map with fitness scores[26] of 0.0566 and 0.0568, respectively. Although the fitness score did not change much (from the initial scores of 0.0573 and 0.0575, respectively) by the refinement docking, the binding pose of MTBD on MT showed some change. The root-mean-square deviation (rmsd) of the refined pose from the initial pose (defined as the all-atom rmsd of the MTDB structure when MT is superimposed) is 5.0 Å for $MTBD_{HA}$ and 7.4 Å for $MTBD_{LA}$. The binding interface residues of MTBD changed by 1.8 and 1.5 Å for $MTBD_{HA}$ and $MTBD_{LA}$, respectively (when MTDB is superimposed), as a result of refinement. As shown in Figure 3, the overall structures of the

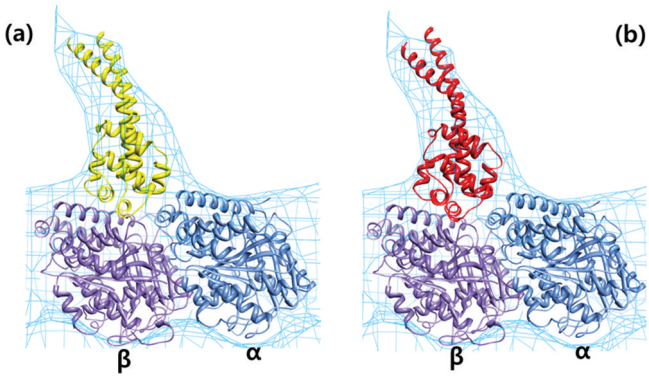

Figure 3. Model structures of the MTBD−MT complex when (a) the low-affinity, crystal MTBD ($MTBD_{LA}$) and (b) the high-affinity, model MTBD ($MTBD_{HA}$) are docked onto MT and refined. Both complex structures fit well to the cryo-EM density map (cyan mesh).[21]

two complexes, $MTBD_{HA}$−MT and $MTBD_{LA}$−MT, obtained by refinement docking are very similar to each other. The all-atom rmsd of MTDB between the high- and low-affinity model structures is 3.1 Å when MT is superimposed. The rmsd of the interface residues of MTBD between the two structures is 2.2 Å.

Before we analyzed the structural changes in detail, we first checked whether the generated model $MTBD_{HA}$ has higher affinity than $MTBD_{LA}$. The relative binding affinity may be estimated by the RosettaDock energy that contains molecular mechanics force field terms such as van der Waals energy, electrostatic energy, solvation free energy, hydrogen bonding energy, etc. The RosettaDock energy for the $MTBD_{HA}$−MT complex structure (−982.8) is indeed lower than that of the $MTBD_{LA}$−MT complex (−980.2), implying that the binding affinity of the $MTBD_{HA}$ model structure is 1.3−2.6 kcal/mol stronger than that of the $MTBD_{LA}$ crystal structure, if the Rosetta energy scale of 0.5−1 kcal/mol[32] is applied. Although typical docking energy is not sufficiently accurate for estimating binding free energy and the results depend on the type of docking energy, this estimation for the binding affinity change agrees well with a recent experimental result in which the binding constant of $MTBD_{HA}$ is roughly 10-fold greater than that of $MTBD_{LA}$.[33] (The Boltzmann factor corresponding to 1.3−2.6 kcal/mol is 9−82 at room temperature.)

The RosettaDock interaction energy decomposes into residue-wise contributions for the amino acid residues at the $MTBD_{HA}$−MT interface (Table S1 of the Supporting Information). It is notable that those electropositive residues of MTBD important for MT binding, as shown in a previous mutagenesis experiment with *Dictyostelium discoideum* dynein,[14] show relatively large contributions to the binding affinity. The prediction for contributions of other residues may also be tested in future experiments. Residue pair interactions responsible for the binding energy are also provided in Table S2 of the Supporting Information.

We notice that the increased binding affinity of $MTBD_{HA}$ compared to that of $MTBD_{LA}$ is due to the increased number of salt bridges. The number of charged hydrogen bonds that are conserved for more than 30% of the simulation time is eleven for the $MTBD_{HA}$−MT complex and nine for the $MTBD_{LA}$−MT complex, involving four and three positively charged residues in MTBD for $MTBD_{HA}$ and $MTBD_{LA}$, respectively.

dx.doi.org/10.1021/bi200834k | *Biochemistry* 2011, 50, 7629−7636

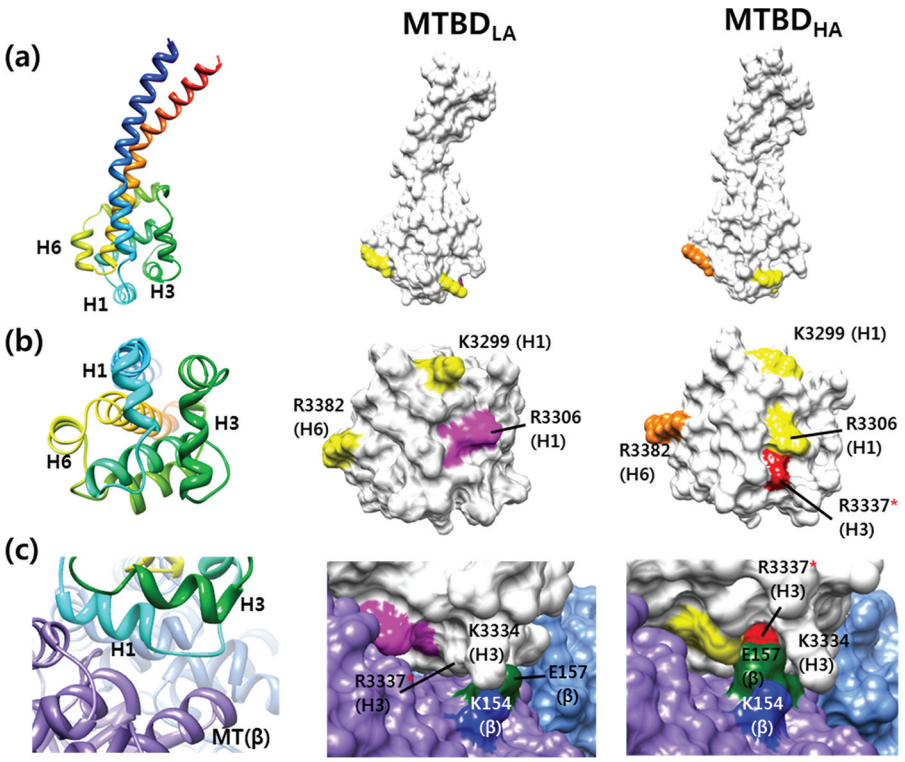

Figure 4. Amino acid residues showing strong salt bridge interactions in the MTBD−MT complex in MD simulations shown (a) on the full structure of MTDB, (b) on the binding interface of MTBD, and (c) together with the β-tubulin near E157. Ribbon diagrams from the same viewpoints (left) are shown together with the surface representations for MTBD$_{LA}$ (middle) and MTBD$_{HA}$ (right). The residues forming one or more charged hydrogen bonds for more than 30% of the simulation time are colored: red for 90−100%, magenta for 80−90%, orange for 60−80%, and yellow for 30−60%. The most striking difference between MTBD$_{LA}$ and MTBD$_{HA}$ is that R3337 at H3 makes strong charged hydrogen bonds with E157 of β-tubulin only in the MTBD$_{HA}$−MT complex. The MTBD$_{HA}$−MT complex also shows better shape complementarity than the MTBD$_{LA}$−MT complex near R3337.

Those residues in MTBD involved in the charge−charge interactions are illustrated in Figure 4.

The complex structure constructed with the low-affinity form of MTBD (MTBD$_{LA}$−MT) shows strong electrostatic interactions at helices H1 (through K3299 and R3306) and H6 (through R3382) (Figure 4b). The same residues also make salt bridges in the high-affinity form (MTBD$_{HA}$−MT) (Figure 4c). We note that the three residues in *D. discoideum* dynein corresponding to K3299, R3306, and R3382 of mouse dynein abolish binding to MT when mutated to alanine.[14] However, the H3 helix, another helix that forms the putative binding interface, does not show strong electrostatic interaction in the MTBD$_{LA}$−MT complex, although mutation of R3337 at H3 to alanine also abolishes binding.

Strikingly, in the MTBD$_{HA}$−MT complex, R3337 at H3 forms a strong salt bridge with E157 of the MT β-unit (Figure 4b,c). This salt bridge maintains charged hydrogen bonds for 90.6% of the simulation time. For comparison, the R3337−E157 pair in the MTBD$_{LA}$−MT complex maintains the charged hydrogen bonds for only 14.2% of the simulation time. In addition to the formation of this salt bridge, the MTDB−MT interface becomes tighter near the R3337−E157 pair, showing better shape complementarity (Figure 4c). The better shape complementarity of the MTBD$_{HA}$−MT complex can also be confirmed by the larger surface area buried by complex formation: 817 Å^2 for the MTBD$_{LA}$−MT complex and 1095 Å^2 for the MTBD$_{HA}$−MT complex. The conformational changes in MTBD that allow the formation of the R3337−E157 salt bridge in the simulation will be discussed in the next section.

Conformational Changes in MTBD Induced by the Registry Shift of the Coiled Coil. The magnitude of the conformational change induced by the registry shift of the coiled-coil stalk is shown in Figure 5a, where the magnitude of the C$_\alpha$ change calculated from the ANM method is plotted. One of the distinctive points in the figure is that the large magnitude of motion (~4.5 Å) at CC1 and CC2 due to the helix sliding is reduced drastically near the proline kinks (P3285 and P3409) at the stalk−MTBD boundary and transformed to relatively smaller changes of <2 Å in the helix bundle. We note that the relative movement of CC1 and CC2 along the coiled-coil axis required for a registry shift by a single helix turn is ~5 Å, but both CC1 and CC2 show rather large changes around 4.5 Å due to additional lateral movements.

The region of the coiled coil near the pair of staggered prolines P3285 and P3409 (shaded in Figure 5a and indicated with a box in Figure 5b) plays the role of "buffer zone" in which the magnitude of helix sliding is modulated. Although the registry shift may be reliably transferred along the well-structured coiled coil of dynein over the long distance of ~15 nm, the extent of the coiled-coil helix motion (~4.5 Å) may not be optimal for modulating the binding affinity of MTBD. If the large helix motion were directly transferred to the helix bundle, the hydrophobic packing of the helix bundle would be disrupted and the whole structure might change completely. However, the motion is absorbed in the buffer zone, and only a fraction of the full motion is transferred to the helix bundle.

How the buffer region works may be understood by examining the interaction network around the region. The registry

dx.doi.org/10.1021/bi200834k | *Biochemistry* 2011, 50, 7629−7636

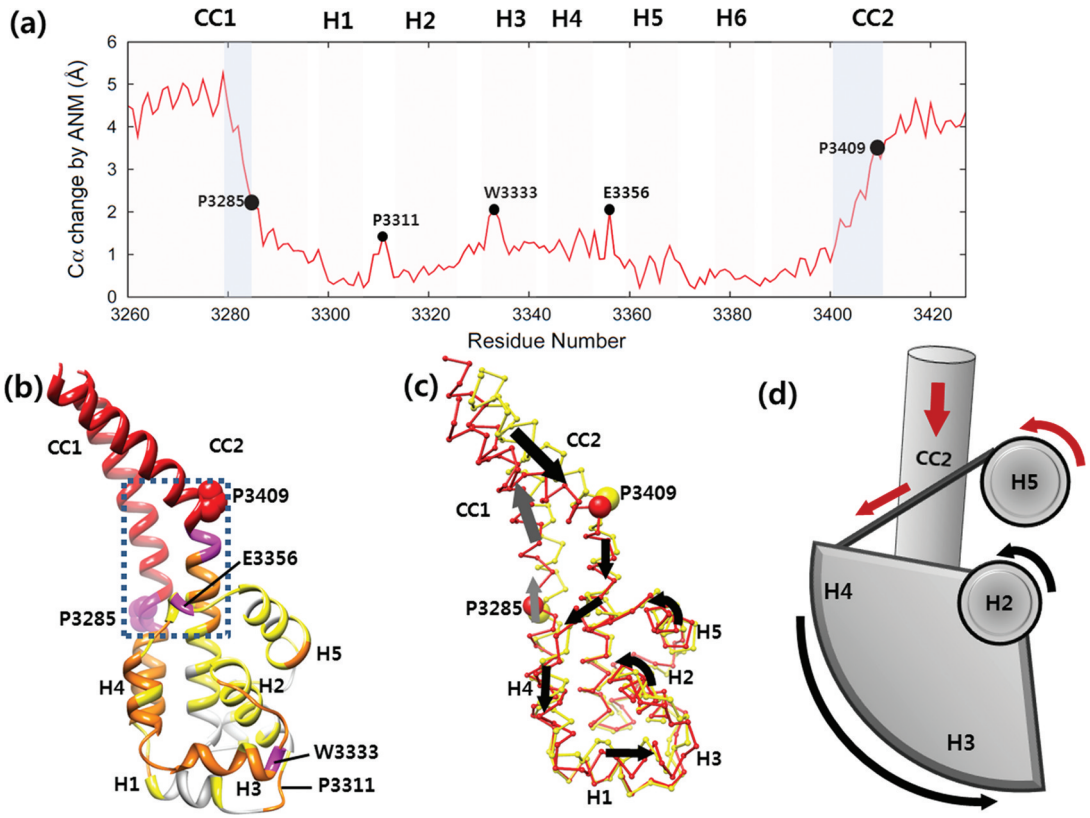

Figure 5. Conformational changes induced by the coiled-coil registry shift. (a) Magnitude of C_α movement for each residue as obtained from the ANM method. The residue range for each substructure (the coiled-coil helices as CC1 and CC2 and the bundle helices as H1−H6) is indicated at the top. The large conformational change (~4.5 Å) of the coiled-coil helices is reduced drastically near the proline kinks (P3285 and P3409) over the shaded buffer region, resulting in changes of <2 Å in the helix bundle. Among the helices forming the binding interface, H1 and H6 show small changes of <1 Å and H3 shows the largest change. The sizes of the changes are also depicted on the crystal structure in panel b with colors: red for >3.0 Å, magenta for 2.0−3.0 Å, orange for 1.0−2.0 Å, yellow for 0.5−1.0 Å, and gray for <0.5 Å. (c) Directions of substructure movements are indicated with arrows on the C_α representations for $MTBD_{LA}$ (yellow) and $MTBD_{HA}$ (red). The large sliding motions of CC1 and CC2 (represented by larger arrows) are reduced near the proline kinks P3285 and P3409, which induce rather small magnitudes of circular motion involving H5, H4, H3, and H2, as indicated with smaller arrows in panel c and shown schematically in panel d.

shift of the coiled coil applies strong strain near the proline kinks because the registry shift cannot be continued because of the helix angle change and the break of the heptad repeat. The weakest point in the interaction network would be broken by the strain, and it turns out to be helix CC1 near P3285. This region of CC1 makes no contact with the helix bundle, while the neighboring residues in CC2 interact with H5 and L4 (the loop connecting H4 and H5). As a result, three backbone hydrogen bonds of the CC1 helix involving K3282 and I3288 are disrupted, and CC1 is unwound near P3285 (indicated with a gray arrow in Figure 5b). Most of the strain due to the registry shift is absorbed near the proline kinks, and the magnitude of the coiled-coil helix sliding continuously decreases below the buffer region of the coiled coil (Figure 5a).

Because the coiled-coil sliding motion is almost fully diminished at the end of the coiled coil, helices H1 and H6 directly connected to CC1 and CC2, respectively, remain the most invariable among the MTBD helices. These two helices, H1 and H6, also contribute to the binding interface, thus making an invariant framework at the binding interface irrespective of the binding state of MTBD.

By contrast, the rest of the MTBD helix bundle is more variable, which can be seen in panels a and b of Figure 5, and serves as an important device for controlling the binding affinity of MTDB. Conformational changes in the helix bundle are shown by comparing the structures of $MTBD_{HA}$ and $MTBD_{LA}$ in Figure 5c and schematically in Figure 5d. Helices that show the largest movements are H3 and H4, and residues that show the largest changes are P3311, W3333, and E3356 (Figure 5a). The roles of P3311 and W3333 are discussed in the next section. The large change at E3356 is due to the contact of the loop (L4) connecting H4 and H5 with CC2 in the buffer region (Figure 5b), where the CC2 sliding is not fully diminished. The closest contact in this area is between A3401 and A3354 (C_α−C_α distance of 5.4 Å). CC2 also makes a close contact with H5 in the buffer region. The downward and lateral movement of CC2 induces downward and lateral movement of the L4 loop and rotation of H5. This initiates counterclockwise rotation of a half-wheel formed by L4, H4, and H3, while H2 plays the role of a pivot. L4, H4, and H3 are roughly on the same plane in space, and H2 is roughly at the center of the half-wheel and perpendicular to the plane of the wheel. The proposed mechanism is schematically drawn in Figure 5d, emphasizing the motions described above and ignoring details to aid understanding. It can be understood that the overall motion is induced as a result of the delicate interaction network formed by the helix bundle and the coiled coil.

Due to the motions of the MTBD helices induced by coiled-coil sliding, the MTBD binding interface formed by H1, H3, and H6 undergoes conformational changes. Only H3 moves

dx.doi.org/10.1021/bi200834k | *Biochemistry* 2011, 50, 7629−7636

significantly, and the other two helices, H1 and H6, remain relatively unchanged. The movement of H3 becomes the most prominent at its N-terminus (~2.4 Å) (Figure 5a,b). Although the magnitude of this movement is not as drastic as in the coiled coil, this is found to be sufficient to cause meaningful atomic-level changes at the binding interface, as discussed in the next section.

It is notable that the proposed conformational change in MTBD affecting the binding affinity is expected not to be very sensitive to the exact magnitude of the CC helix sliding motion because the downward helix sliding motion can be almost fully absorbed in the buffer zone by breaking hydrogen bonds. The magnitude of the binding interface change can then be controlled by the delicate interaction network of the helix bundle itself and the W3333–P3311 interaction, as suggested below.

Roles of W3333 and P3311 Residues in Regulating Binding Affinity. How is the 2.4 Å movement of H3 in MTBD related to the formation of a new salt bridge with MT? Through the analyses of the MD simulation trajectories, we found that this question can be answered in a quantitative manner. The key interaction seems to be that between W3333 and P3311, which also show the largest movements upon the coiled-coil registry shift. W3333 is located at the N-terminus of H3, and P3311 is in the linker connecting H1 and H2 (Figure 5b). W3333 and P3311 are two of the most highly conserved nonpolar residues in the dynein family, implying that these residues are critical for MTBD function. However, the molecular basis of their role is unknown.

Table 1. Structural Features of the MTBD–MT Complex for Low- and High-Affinity Forms of Native MTBD and the W3333A Mutant

	$MTBD_{LA}$–MT	$MTBD_{HA}$–MT	W3333A–MT
average W3333 RSA[a] (%)	8.01 (3.00)	47.73 (6.79)	33.63 (21.43)
R3337–E157 salt bridge[b] (%)	14.21	90.64	0.91
average W3333–P3311 distance[c] (Å)	6.02 (0.59)	6.23 (0.71)	7.67 (1.43)
rmsf of H3[d] (Å)	1.12	1.24	1.83

[a]Relative surface area averaged over the simulation time. The standard deviation is given in parentheses. The relative surface area is the surface area relative to that of the fully exposed state. [b]Percentage of the simulation time during which the charged hydrogen bonds making the salt bridge are maintained. [c]Average C_β–C_β distance between W3333 (or A3333 for W3333A) and P3311. [d]Average root-mean-square-fluctuations of H3 residues (W3333–M3341).

As summarized in Table 1, W3333 of $MTBD_{LA}$ is buried well inside the hydrophobic core during simulation with an average relative surface area (RSA) of 8.0%. By contrast, W3333 in $MTBD_{HA}$ becomes exposed to solvent (RSA = 47.7%). Note that these values are statistically significant with small standard deviations (3.0 and 6.8%, respectively), implying that the tryptophan residue is in stable states. The side chain of W3333 closely interacts with P3311 and packed into the protein core in $MTBD_{LA}$ (Figure 6a), and it undergoes an abrupt change in orientation and is exposed to the protein surface when H3 sliding occurs in $MTBD_{HA}$ (Figure 6b). W3333 still interacts closely with P3311 in $MTBD_{HA}$.

The most remarkable change coupled with the W3333 movement is the change in orientation of the R3337 side chain. The space occupied by W3333 in $MTBD_{LA}$ becomes available in $MTBD_{HA}$, and the R3337 side chain buries some of its aliphatic atoms there. The concerted movement of H3 sliding and the R3337 side chain angle change allow formation of a new salt bridge with E157 of the MT β-unit (Table 1), improving both geometric and electrostatic complementarity, as described in the legend of Figure 4c.

We propose that the W3333–P3311 contact plays the role of holding H3 at a proper position in the low- and high-affinity states. In our simulations, the W3333–P3311 stacking interaction remains stable in $MTBD_{LA}$ and $MTBD_{HA}$, as can be seen from the small W3333–P3311 distance and its standard deviation in Table 1. If W3333 is mutated to alanine, the A3333–P3311 contact is broken and the A3333–P3311 distance and its standard deviation increase. The loss of the W3333–P3311 interaction results in an increase in the root-mean-square fluctuations at H3 in the W3333A mutant (Table 1), leading to destabilization of the R3337–E157 (MT β) salt bridge (Figure 6c). The H3 movement of 2.4 Å seems to be large enough to switch the W3333 state from the buried to the exposed state but small enough at the same time to maintain the W3333–P3311 stacking to hold the H3 position. Therefore, the W3333–P3311 interaction plays the role of a switch to turn on and off the R3337–E157 (MT β)

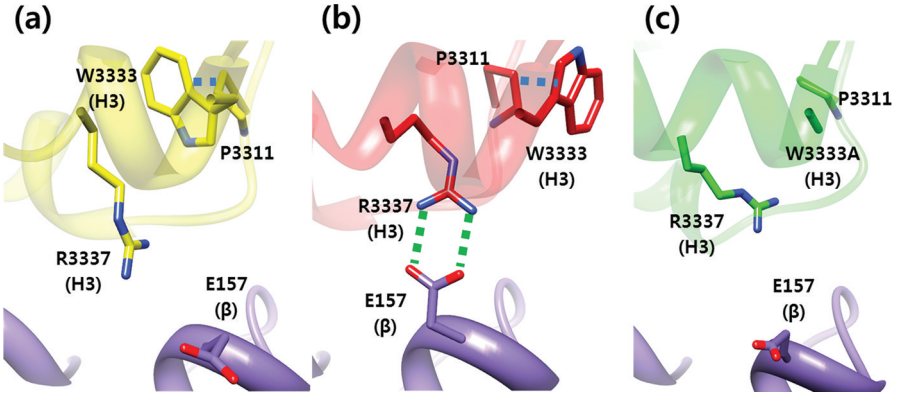

Figure 6. Snapshot structures from MD simulations that show key residues involved in the formation of a new salt bridge between MTDB and MT for the (a) $MTBD_{LA}$–MT, (b) $MTBD_{HA}$–MT, and (c) W3333A–MT complexes. The stacking interaction between W3333 and P3311 and the charged hydrogen bonding interaction between R3337 (H3) and E157 (MT β) are indicated with dashed lines. This figure highlights the importance of the W3333–P3311 interaction as a toggle switch for salt bridge formation.

dx.doi.org/10.1021/bi200834k | *Biochemistry* 2011, 50, 7629–7636

salt bridge interaction and at the same time the role of a linchpin to hold the interfacial helix H3.

CONCLUSIONS

In this study, we generated a molecular model structure for the high-affinity form of dynein MTBD with a registry shift and its complex structure with MT. This modeling study was conducted by combining computational methods and available experimental data. The model MTBD structure with the registry shift shows higher binding affinity for MT than the crystal structure for a low-affinity form by forming a new salt bridge with MT. The mechanism by which the registry shift of the coiled-coil stalk is relayed to MTBD could be explained mostly in terms of the atomic interaction network of the protein. Roles of substructures (helices and loops) are explained in a consistent manner. The proposed mechanism based on our model structures also explains the roles of the highly conserved residues revealed in a previous mutagenesis study. In this study, we focused on binding of MTDB with MT and questions about how the current picture of MTDB conformational changes can be incorporated into the bigger picture of dynein function; for example, the question of how the conformational changes of MTBD affect communications with the rest of dynein remains to be answered.

ASSOCIATED CONTENT

Supporting Information

Tabulated summaries of the RosettaDock interaction energies decomposed into residue-wise contributions (Table S1) and residue pair interactions (Table S2) for residues at the $MTBD_{HA}$−MT interface. This material is available free of charge via the Internet at http://pubs.acs.org.

Accession Codes

Accession codes: PDB entry 3ERR, PDB entry 1JFF, and EMDB entry 1581.

AUTHOR INFORMATION

Corresponding Author

*Phone: +82-2-880-9197. E-mail: chaok@snu.ac.kr. Fax: +82-2-871-8119.

Funding

This work was supported by KOSEF/MEST Grant 2011-0012456.

ACKNOWLEDGMENTS

We thank Prof. Steven Gross for discussions in the early stages of this work.

ABBREVIATIONS

MT, microtubule(s); MTBD, microtubule-binding domain; $MTBD_{HA}$, high-affinity state of MTBD; $MTBD_{LA}$, low-affinity state of MTBD; AAA+, ATPases associated with diverse cellular activities; CC, coiled coil; CC1, one of the CC helices that extends from AAA+ to MTBD; CC2, another CC helix that extends from MTBD to AAA+; cryo-EM, cryo-electron microscopy; ANM, anisotropic network model; MD, molecular dynamics; PDB, Protein Data Bank; EMDB, Electron Microscopy Data Bank; RSA, relative surface area; rmsd, root-mean-square deviation.

REFERENCES

(1) Gibbons, I. R., and Rowe, A. J. (1965) Dynein: A protein with adenosine triphosphatase activity from cilia. *Science 149*, 424−426.

(2) Paschal, B. M., and Vallee, R. B. (1987) Retrograde transport by the microtubule-associated protein MAP 1C. *Nature 330*, 181−183.

(3) DiBella, L. M., and King, S. M. (2001) Dynein motors of the *Chlamydomonas* flagellum. *Int. Rev. Cytol. 210*, 227−268.

(4) Vale, R. D. (2003) The molecular motor toolbox for intracellular transport. *Cell 112*, 467−480.

(5) Vallee, R. B., Williams, J. C., Varma, D., and Barnhart, L. E. (2004) Dynein: An ancient motor protein involved in multiple modes of transport. *J. Neurobiol. 58*, 189−200.

(6) Gee, M. A., and Heuser, J. (1997) An extended microtubule-binding structure within the dynein motor domain. *Nature 390*, 636−639.

(7) Carter, A. P., Garbarino, J. E., Wilson-Kubalek, E. M., Shipley, W. E., Cho, C., Milligan, R. A., Vale, R. D., and Gibbons, I. R. (2008) Structure and Functional Role of Dynein's Microtubule-Binding Domain. *Science 322*, 1691−1695.

(8) Hagezparast, M., Klock, R., Ruhrberg, C., Marquardt, A., Ahmad-Annuar, A., Bowen, S., Lalli, G., Witherden, A. S., Hummerich, H., Nicholson, S., Morgan, P. J., Oozageer, R., Priestley, J. V., Averill, S., King, V. R., Ball, S., Peters, J., Toda, T., Yamamoto, A., Hiraoka, Y., Augustin, M., Korthaus, D., Wattler, S., Wabnitz, P., Dickneite, C., Lampel, S., Boehme, F., Peraus, G., Popp, A., Rudelius, M., Schlegel, J., Fuchs, H., de Angelis, M. H., Schiavo, G., Shima, D. T., Russ, A. P., Stumm, G., Martin, J. E., and Fisher, E. M. C. (2003) Mutation in dynein linker motor neuron degeneration to defects in retrograde transport. *Nature 300*, 808−812.

(9) Zuccarello, D., Ferlin, A., Cazzadore, C., Pepe, A., Moretti, A., Cordeschi, G., Francabilla, S., and Foresta, C. (2008) Mutations in dynein genes in patients affected by isolated non-syndromic asthenozoosperimia. *Hum. Reprod. 23*, 1957−1962.

(10) Lowe, J., Li, H., Downing, K. H., and Nogales, U. K. (2001) Refined structure of $\alpha\beta$-tubulin at 3.5 Å resolution. *J. Mol. Biol. 313*, 1045−1057.

(11) Mizuno, N., Toba, S., Edamatsu, M., Watai-Nishii, J., Hirokawa, N., Toyoshima, Y. Y., and Kikkawa, M. (2004) Dynein and kinesin share on overlapping microtubule-binding site. *EMBO J. 23*, 2459−2467.

(12) Kon, T., Imamura, K., Roberts, A. J., Ohkura, R., Knight, P. J., Gibbons, I. R., Burgess, S. A., and Sutoh, K. (2009) Helix sliding in the stalk coiled coil of dynein couples ATPase and microtubule binding. *Nat. Struct. Mol. Biol. 16*, 325−333.

(13) Gibbons, I. R., Garbarino, J. E., Tan, C. E., Reck-Peterson, S. L., Vale, R. D., and Carter, A. P. (2005) The affinity of the dynein microtubule-binding domain is modulated by the conformation of its coiled-coil stalk. *J. Biol. Chem. 280*, 23960−23965.

(14) Koonce, M. P., and Tikhonenko, I. (2000) Functional Elements within the Dynein Microtubule-binding Domain. *Mol. Biol. Cell 11*, 523−529.

(15) Woehlke, G., Ruby, A. K., Hart, C. L., Ly, B., Hom-Booher, N., and Vale, R. D. (1997) Microtubule interaction site of the kinesin motor. *Cell 90*, 207−216.

(16) Atilgan, A. R., Durell, S. R., Jernigan, R. L., Demirel, M. C., Keskin, O., and Bahar, I. (2001) Anisotropy of Fluctuation Dynamics of Proteins with an Elastic Network Model. *Biophys. J. 80*, 505−515.

(17) Eyal, E., Yang, L. W., and Bahar, I. (2006) Anisotropic network model: Systematic evaluation and a new web interface. *Bioinformatics 22*, 2619−2627.

(18) Miyazawa, S., and Jernigan, R. L. (1985) Estimation of Effective Interresidue Contact Energies from Protein Crystal Structures: Quasi-Chemical Approximation. *Macromolecules 18*, 534−552.

(19) Miyashita, O., Onuchic, J. N., and Wolynes, P. G. (2003) Nonlinear elasticity, proteinquakes, and the energy landscapes of

functional transitions in proteins. *Proc. Natl. Acad. Sci. U.S.A. 100*, 12570−12575.

(20) Sali, A., and Blundell, T. L. (1993) Comparative protein modeling by satisfaction of spatial restraints. *J. Mol. Biol. 234*, 779−815.

(21) Lawson, C. L., Baker, M. L., Best, C., Bi, C., Dougherty, M., Feng, P., Ginkel, G., Devkota, B., Lagerstedt, I., Ludtke, S. J., Newman, R. H., Oldfield, T. J., Rees, I., Sahni, G., Sala, R., Velankar, S., Warren, J., Westbrook, J. D., Henrick, K., Kleywegt, G. J., Berman, H. M., and Chiu, W. (2011) EMDataBank.org: Unified data resource for CryoEM. *Nucleic Acids Res. 39*, D456−D464.

(22) Gray, J. J., Moughon, S., Wang, C., Scueler-Furman, O., Rohl, C. A., and Baker, D. (2003) Protein-Protein Docking with Simultaneous Optimization of Rigid-body Displacement and Side-chain Conformations. *J. Mol. Biol. 331*, 281−299.

(23) Li, Z., and Scheraga, H. A. (1987) Monte Carlo-minimization approach to the multiple-minima problem in protein folding. *Proc. Natl. Acad. Sci. U.S.A. 84*, 6611−6615.

(24) Kirkpatrick, S., Gelatt, C. D., and Vecchi, M. P. (1983) Optimization by Simulated Annealing. *Science 220*, 671−680.

(25) Kortemme, T., Morozov, A. V., and Baker, D. (2003) An Orientation-dependent Hydrogen Bonding Potential Improves Prediction of Specificity and Structure for Proteins and Protein−Protein Complexes. *J. Mol. Biol. 326*, 1239−1259.

(26) Hasel, W., Hendrickson, T. F., and Still, W. C. (1988) A rapid approximation to the Solvent Accessible Surface Area of Atoms. *Tetrahedron Comput. Methodol. 1*, 103−116.

(27) Wriggers, W. (2010) Using *Situs* for the integration of multi-resolution structures. *Biophys. Rev. 2*, 21−27.

(28) Case, D. A., Darden, T. A., Cheatham, T. E., III, Simmerling, C. L., Wang, J., Duke, R. E., Luo, R., Crowley, M., Walker, R. C., Zhang, W., Merz, K. M., Wang, B., Hayik, S., Roitberg, A., Seabra, G., Kolossváry, I., Wong, K. F., Paesani, F., Vanicek, J., Wu, X., Brozell, S. R., Steinbrecher, T., Gohlke, H., Yang, L., Tan, C., Mongan, J., Hornak, V., Cui, G., Mathews, D. H., Seetin, M. G., Sagui, C., Babin, V., and Kollman, P. A. (2008) *AMBER 10*, University of California, San Francisco.

(29) Berendsen, H. J. C., Postma, J. P. M., van Gunsteren, W. F., DiNola, A., and Haak, J. R. (1984) Molecular dynamics with coupling to an external bath. *J. Chem. Phys. 81*, 3684−3690.

(30) Ryckaert, J. P., Catarello, D. P., and Wozniak, J. M. (1977) Numerical integration of the Cartesian equations of motion of a system with constraints: Molecular dynamics of n-alkanes. *J. Comput. Phys. 23*, 327−341.

(31) Jorgensen, W. L., Chandrasekhar, J., Madura, J. D., Impey, R. W., and Klein, M. L. (1983) Comparison of simple potential functions for simulating liquid water. *J. Chem. Phys. 79*, 926−935.

(32) Kortemme, T., Kim, D. E., and Baker, D. (2004) Computational Alanine Scanning of Protein-Protein interfaces. *Sci. STKE 219*, pl2.

(33) Carter, A. P., and Vale, R. D. (2010) Communication between the AAA+ ring and microtubule-binding domain of dynein. *Biochem. Cell Biol. 88*, 15−21.